ACS APPLIED MATERIALS & INTERFACES

Letter

Cite This: ACS Appl. Mater. Interfaces 2018, 10, 14287−14291

www.acsami.org

Dynamic Adsorption of CO_2/N_2 on Cation-Exchanged Chabazite SSZ-13: A Breakthrough Analysis

Jamey K. Bower,[†,§] Dushyant Barpaga,[‡] Sebastian Prodinger,[†] Rajamani Krishna,[⊥] H. Todd Schaef,[†] B. Peter McGrail,[‡] Miroslaw A. Derewinski,*[,†] and Radha Kishan Motkuri*[,‡]

[†]Physical and Computational Sciences Division, Pacific Northwest National Laboratory (PNNL), Richland, Washington 99352, United States

[‡]Energy and Environment Directorate, Pacific Northwest National Laboratory (PNNL), Richland, Washington 99352, United States

[§]Department of Chemistry and Biochemistry, The Ohio State University, Columbus, Ohio 43210, United States

[⊥]Van't Hoff Institute for Molecular Sciences, University of Amsterdam, Science Park 904, 1098 XH Amsterdam, The Netherlands

Supporting Information

ABSTRACT: Alkali-exchanged SSZ-13 adsorbents were investigated for their applicability in separating N_2 from CO_2 in flue gas streams using a dynamic breakthrough method. In contrast to IAST calculations based on equilibrium isotherms, K^+ exchanged SSZ-13 was found to yield the best N_2 productivity, comparable to Ni-MOF-74, under dynamic conditions where diffusion properties play a significant role. This was attributed to the selective, partial blockage of access to the chabazite cavities, enhancing the separation potential in a 15/85 CO_2/N_2 binary gas mixture.

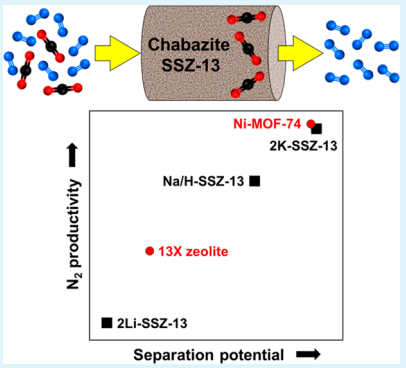

KEYWORDS: *chabazite, SSZ-13, dynamic adsorption, breakthrough, cation-exchange*

The release of carbon dioxide (CO_2) from anthropogenic point sources, such as coal-fired power plants or conventional cooling systems, accounts for approximately 35% of total CO_2 emissions in the United States and is linked to climate change.[1−3] Postcombustion capture of carbon dioxide can reduce these emissions, but hinges on the separation of CO_2 from a flue gas mixture containing primarily nitrogen, carbon dioxide, water vapor, and oxygen.[4] Using adsorbent materials to remove CO_2 from flue gas is advantageous due to its low energy penalty for loading and regeneration in addition to the existence of infrastructure to support its incorporation into the exhaust system of power plants.[5,6] Various nanoporous materials such as zeolites, metal−organic frameworks, covalent organic frameworks, and hierarchical porous carbons have been explored for CO_2 adsorption and separation studies.[7−12] Among them, nanoporous zeolites have received significant attention because of their robust nature, economical preparations, and very high thermal and chemical stabilities.[13−15]

SSZ-13 (CHA) zeolites have gained notoriety over other zeolites for their high affinity toward carbon dioxide over other gases because of its unique pore structure and arrangement of cations in the framework.[14,16] Increasing the electrostatic interaction between the framework and the CO_2 guest molecules by altering the Si/Al ratio, the nature of extra-framework cations, as well as the particle size, can improve adsorption properties. Such alterations make these zeolites excellent molecular sieves capable of separating CO_2 (3.3 Å) from N_2 (3.6 Å) in flue gas streams.[17,18] Additional modifications involving the use of larger cations, such as potassium and cesium in low silica CHA, were found to yield even higher selectivities of CO_2 over N_2. This was due mainly to a molecular trapdoor mechanism, which discriminates guest molecules by their interaction with host cations, and not necessarily based on size alone.[19] These studies focusing on the nature of metal cations have been largely limited to equilibrium measurements.[20,21]

In an industrial setting, the capture of CO_2 from flue gas is typically carried out in fixed bed adsorbers under dynamic conditions whose separation performance is dictated by a combination of selectivity and capacity. For this reason, breakthrough measurements are more representative of practical separations and limited research has focused in this direction.[22−24] Here we identify a suitable SSZ-13 candidate for separating a CO_2/N_2 gas mixture based on its separation potential and N_2 productivity as it compares with traditional benchmark sorbents. The intent of this study is to explore the

Received: March 7, 2018
Accepted: April 17, 2018
Published: April 17, 2018

DOI: 10.1021/acsami.8b03848
ACS Appl. Mater. Interfaces 2018, 10, 14287−14291

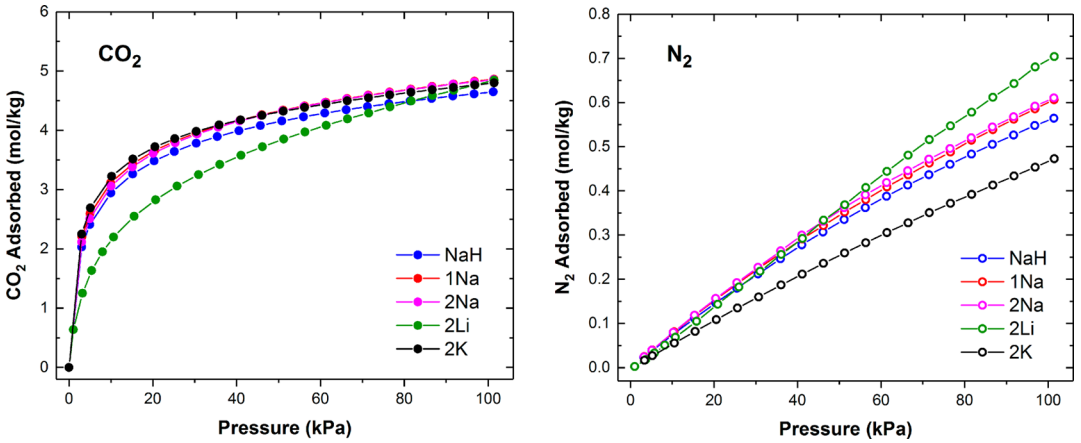

Figure 1. Equilibrium CO_2 and N_2 adsorption isotherms at 298 K for the cation-exchanged SSZ-13 samples. Lines are drawn to guide the eyes.

effect of alkali cation exchange on CO_2/N_2 separation. Specifically, the location and quantity of cations in the pores of chabazite SSZ-13 will be correlated to differences in adsorption of CO_2 vs N_2 via breakthrough experiments.

On the basis of our previous contribution,[18,25] we used submicron SSZ-13 of Si/Al = 5 as a starting material, which provided a superior CO_2 adsorption potential compared to traditionally synthesized SSZ-13 of larger dimensions due to the number of adsorption sites. To exploit the strong interactions between the Lewis basic oxygens of CO_2 and the Lewis acidic cations in the framework, we performed a number of exchanges with alkali cations (Li, Na, and K) on the starting material (Na/H) (Figure S2). An illustration of a section of the SSZ-13 framework structure with various potential sites of cation incorporation is shown in Figure 2 (inset). Elemental analysis (Table S1) of the highly crystalline SSZ-13 prior to any additional ionic exchanges showed a Na/Al of 0.6 with the remaining Al balanced by protons. The cation exchange degree was increased by repeating the number of exchanges such that 0.7 (1Na-SSZ-13) and ca. 0.8 (2Na-SSZ-13) were obtained, respectively, with protons balancing the residual framework charge. The micropore volume as well as the corresponding specific surface areas ranged between 0.22 and 0.27 cm^3/g and 600−750 m^2/g, respectively (Table S1 and Figures S3 and S4). The pore size distribution of the microporous regime reflected the internal dimensions of the SSZ-13 cage known to be 7.3 Å × 12 Å. The sample exchanged with larger cations, K^+ (r = 1.5 Å), presented a slightly smaller pore volume and surface area. This can be attributed to apparent pore blocking, also evidenced by the appearance of a minor contribution of pores between 16 and 18 Å, which we assign to the equilibration of N_2 in insterstital pores between the crystallites. This is due to the larger size of the K^+ as well as its preferential location in the center of the eight membered-ring (8MR).[26]

Unary CO_2 and N_2 equilibrium (static) adsorption isotherms, shown in Figure 1, for the cation exchanged zeolites showed slightly improved behavior compared to previously reported SSZ-13 materials (Na/H).[17] A maximum uptake of ∼5.0 mol/kg at a pressure of ca. 100 kPa was achieved for all cation exchanged samples. On the contrary, N_2 isotherms with much lower affinity (less uptake) were observed for the same samples with a maximum uptake of ∼0.8 mol/kg at 100 kPa (Figures S5−S7). The resulting heat of adsorption for CO_2 (Table S2) was found to be approximately 40 kJ/mol, which is in line with previously published data on alkali-exchanged SSZ-13.[17]

Using the ideal adsorbed solution theory (IAST), unary equilibrium isotherms for CO_2 and N_2 were used to predict the behavior in a binary gas mixture (15/85 CO_2/N_2) (Tables S3 and S4), where this ratio was chosen based on CO_2 content of harsh simulated flue gas conditions as reported in prior literature.[27] The resulting adsorption selectivity (S_{ads}) correlated to volumetric CO_2 (Q_{CO2}) uptakes are shown in Figure 2

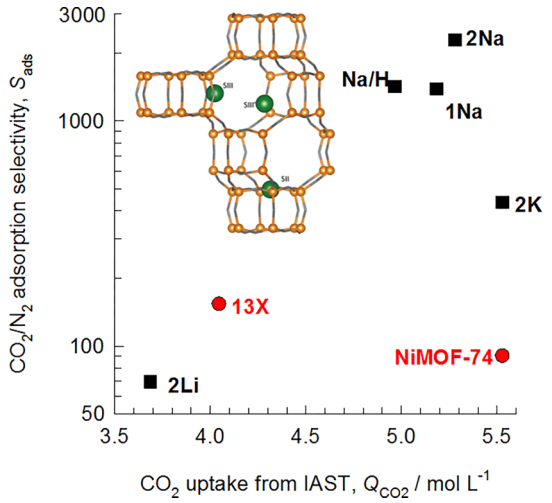

Figure 2. CO_2/N_2 adsorption selectivities determined using IAST calculations (black) from equilibrium adsorption isotherms as a function of volumetric CO_2 uptake for a 15/85 CO_2/N_2 gas mixture at 298 K and 100 kPa. Benchmark materials for CO_2 adsorption (red), 13X zeolite, and Ni-MOF-74 are also included for comparison. The inset shows a depiction of the CHA zeolite framework consisting of three double six-membered-ring units. Potential sites where cations can be incorporated in the framework are shown. These sites are labeled SII, SIII, and SIII′ as per Pham et al.[17]

and compared to benchmark adsorbents, 13X and NiMOF-74 (Tables S5−S8).[28] These data, showcased by the exchange with Na^+, suggest that increasing the exchange degree and inversely decreasing the concentration of H^+ (very poor interaction with CO_2) can improve both the selectivity of adsorption as well as the uptake of CO_2. However, the highest CO_2 uptake is obtained using the 2K-SSZ-13 sample, which we attribute to dual cation sites in location SIII′ (the 8MR window) and SII

DOI: 10.1021/acsami.8b03848
ACS Appl. Mater. Interfaces 2018, 10, 14287−14291

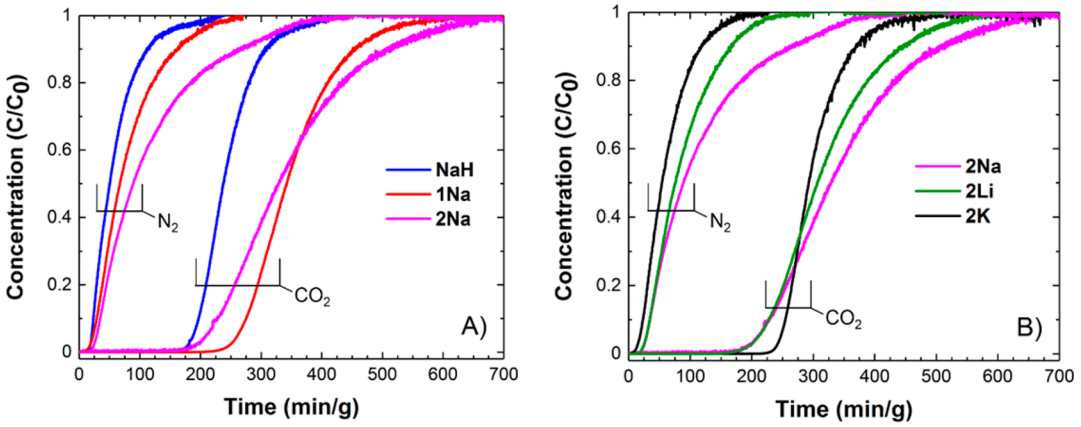

Figure 3. Dynamic adsorption profiles using a CO_2/N_2 gas mixture from breakthrough measurements. (A) Breakthrough profiles for SSZ-13 samples with varying Na concentration. (B) Breakthrough profiles for SSZ-13 samples with varying cations.

that are able to bind a larger number of CO_2.[10] On the other hand, Na^+ is located primarily in SII (near the window of the double six-membered ring). This is also the case for Li^+, which, despite having a stronger electric field, exhibits the lowest selectivity because of a stronger electrostatic association for N_2.[29,30] When coupled with the apparent lower affinity for CO_2 at low pressures, the result is a poor separation of the binary mixture using Li^+ exchanged SSZ-13. In contrast to the benchmark materials, 13X and Ni-MOF-74, the other cation-exchanged SSZ-13 samples performed significantly better. We speculate that advantages over the inaccessible cations in sodalite cages of 13X zeolite and the nonselective adsorption by unsaturated metal sites of a large pore volume Ni-MOF-74 lead to the improvements in CO_2 selectivities observed by our SSZ-13 samples.

The main focus of this contribution, however, is the evaluation of cation-exchanged SSZ-13 in dynamic conditions represented by binary, breakthrough (dynamic) adsorption profiles using a 15/85 CO_2/N_2 gas mixture as depicted in Figure 3. Consistent with equilibrium isotherms, higher affinity of SSZ-13 for CO_2 over N_2 leads to sufficiently long differences in breakthrough times for all investigated materials. Slight differences compared to equilibrium isotherms and resultant IAST calculations are, however, observed when investigating increasing Na^+ concentrations (Figure 3A). This can be gathered from the distended nature of breakthroughs (e.g., 2Na), caused due to a variety of reasons such as axial dispersion, intracrystalline diffusion, and finite selectivities. For SSZ-13 materials, intracrystalline diffusion effects are of particular importance because the molecules need to diffuse through narrow 8-ring windows of 3.8 Å × 4.2 Å separating adjacent cages. When investigating the type of cation (Figure 3B), the same observation can be made with both 2Na and 2Li having more distended breakthrough curves compared to 2K. Under these dynamic conditions, the resulting CO_2 capacities (Table S9) were also significantly lower than those obtained from equilibrium uptakes.

However, a more important characteristic of these breakthrough experiments is the N_2 productivity, which describes the amount of pure N_2 that can be collected at the outlet in a single pass. This value is intricately linked to the separation potential (eq 1). The latter can be calculated using the Shock wave model and volumetric uptakes assuming that the maximum achievable productivity of pure N_2 is realized when both intracrystalline diffusion and axial dispersion effects are completely absent and the concentrations "fronts" of the fluid mixture traverse the fixed bed in the form of shock waves.[31]

$$\Delta Q = \left(Q_{CO2} \frac{y_{N2}}{1 - y_{N2}} - Q_{N2} \right) \quad (1)$$

In practice, the productivities will be lower than the calculated ΔQ values due to the effects described above resulting in a distended breakthrough. Therefore, more representative transient breakthrough simulations for 15/85 CO_2/N_2 mixtures at 298 K and 100 kPa were performed using the methodology described in detail in the literature.[28] All breakthrough experiments could be simulated with good accuracy (Figures S8–S10) with the same set of values for intracrystalline diffusivities.

Figure 4 presents a plot of the productivity in a fixed bed (requiring at least 99.95% pure N_2 as assessed by a material balance) as a function of the corresponding values of the separation potential ΔQ, as determined earlier. It is interesting to note that the best performing adsorbent (i.e., 2Na-SSZ-13) with the highest selectivity from equilibrium based IAST calculations (Figure 2) is outperformed by both the 1Na and

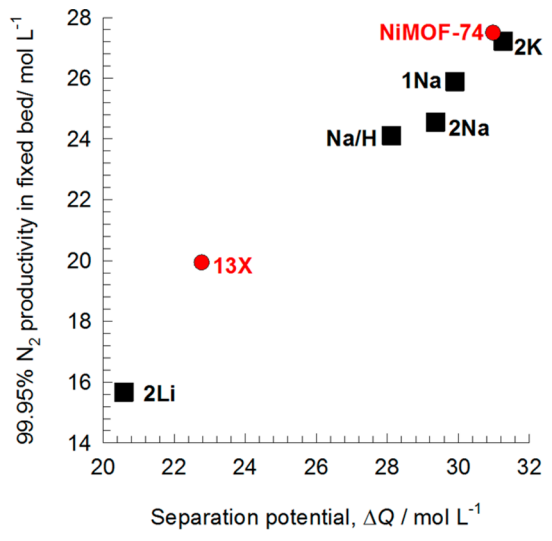

Figure 4. N_2 productivity as a function of the separation potential, ΔQ, for the various cation-exchanged SSZ-13 zeolites in comparion with benchmark adsorbents Ni-MOF-74 and 13X.

DOI: 10.1021/acsami.8b03848
ACS Appl. Mater. Interfaces 2018, 10, 14287−14291

even more so by the 2K-SSZ-13 sample. We speculate that this discrepancy originates from a higher concentration of cations as well as different locations of these cations within the zeolite pores, thus affecting the diffusion. Specifically in the case of 2K-SSZ-13, the possible location of K^+ in the 8MR windows would block access to the SSZ-13 cavity for less polar N_2 compared to CO_2 ("trapdoor effect"),[19] leading to the observed N_2 productivity on par with Ni-MOF-74. Although this trapdoor effect is usually observed for Si/Al < 3, given the expected blocking of all 8MR with large cations (e.g., K^+, Rb^+ or Cs^+),[21] we postulate that under dynamic conditions, even incomplete blocking of all cages can still significantly affect the diffusion through the zeolite crystals and thus the N_2 productivity.

In conclusion, we found that equilibrium-based IAST calculations are inadequate to assess the potential of our adsorbents for industrial applications. These processes are more accurately described by breakthrough experiments, which showed potential suitability of K^+ exchanged SSZ-13 as an efficient adsorbent for CO_2 separation based upon the trapdoor behavior of potassium ions blocking access to SSZ-13 cavities.

■ ASSOCIATED CONTENT

Supporting Information

The Supporting Information is available free of charge on the ACS Publications website at DOI: 10.1021/acsami.8b03848.

Experimental details: synthesis procedures, XRD, NMR, porosimetry, TGA-MS, ICP-MS, equilibrium and dynamic adsorption experiments, IAST calculations, and transient modeling (PDF)

■ AUTHOR INFORMATION

Corresponding Authors

*E-mail: Radhakishan.Motkuri@pnnl.gov. Tel: +1 (509) 371-6484. +1 (509) 375-3856.
*E-mail: Miroslaw.Derewinski@pnnl.gov.

ORCID

Dushyant Barpaga: 0000-0003-2271-6213
Sebastian Prodinger: 0000-0001-8749-0476
Rajamani Krishna: 0000-0002-4784-8530
H. Todd Schaef: 0000-0002-4546-3979
Miroslaw A. Derewinski: 0000-0003-1738-2247
Radha Kishan Motkuri: 0000-0002-2079-4798

Notes

The authors declare no competing financial interest.

■ ACKNOWLEDGMENTS

The authors acknowledge Office of Fossil Energy for the support. J.K.B. thanks the U.S. Department of Energy, Office of Science, Office of Workforce Development for Teachers and Scientists (WDTS), and Science Undergraduate Laboratory Internships Program (SULI) at Pacific Northwest National Laboratory (PNNL). S.P and M.A.D. acknowledge support by PNNL's Materials Synthesis and Simulation Across Scales (MS^3 Initiative) conducted under the Laboratory Directed Research & Development Program. PNNL is operated by Battelle for the U.S. Department of Energy (DOE) under Contract DE-AC05-76RL01830.

■ REFERENCES

(1) Boot-Handford, M. E.; Abanades, J. C.; Anthony, E. J.; Blunt, M. J.; Brandani, S.; Mac Dowell, N.; Fernandez, J. R.; Ferrari, M. C.; Gross, R.; Hallett, J. P.; Haszeldine, R. S.; Heptonstall, P.; Lyngfelt, A.; Makuch, Z.; Mangano, E.; Porter, R. T. J.; Pourkashanian, M.; Rochelle, G. T.; Shah, N.; Yao, J. G.; Fennell, P. S. Carbon capture and storage update. *Energy Environ. Sci.* **2014**, *7* (1), 130−189.
(2) Gibbins, J.; Chalmers, H. Carbon capture and storage. *Energy Policy* **2008**, *36* (12), 4317−4322.
(3) Zheng, J.; Vemuri, R. S.; Estevez, L.; Koech, P. K.; Varga, T.; Camaioni, D. M.; Blake, T. A.; McGrail, B. P.; Motkuri, R. K. Pore-Engineered Metal-Organic Frameworks with Excellent Adsorption of Water and Fluorocarbon Refrigerant for Cooling Applications. *J. Am. Chem. Soc.* **2017**, *139* (31), 10601−10604.
(4) Kanniche, M.; Le Moullec, Y.; Authier, O.; Hagi, H.; Bontemps, D.; Neveux, T.; Louis-Louisy, M. Up-to-date CO2 capture in thermal power plants. *Energy Procedia* **2017**, *114*, 95−103.
(5) Samanta, A.; Zhao, A.; Shimizu, G. K. H.; Sarkar, P.; Gupta, R. Post-Combustion CO2 Capture Using Solid Sorbents: A Review. *Ind. Eng. Chem. Res.* **2012**, *51* (4), 1438−1463.
(6) Lee, S. Y.; Park, S. J. A review on solid adsorbents for carbon dioxide capture. *J. Ind. Eng. Chem.* **2015**, *23*, 1−11.
(7) Trickett, C. A.; Helal, A.; Al-Maythalony, B. A.; Yamani, Z. H.; Cordova, K. E.; Yaghi, O. M. The chemistry of metal-organic frameworks for CO2 capture, regeneration and conversion. *Nat. Rev. Mater.* **2017**, *2* (8), 17045.
(8) Estevez, L.; Barpaga, D.; Zheng, J.; Sabale, S.; Patel, R. L.; Zhang, J. G.; McGrail, B. P.; Motkuri, R. K. Hierarchically Porous Carbon Materials for CO2 Capture: The Role of Pore Structure. *Ind. Eng. Chem. Res.* **2018**, *57* (4), 1262−1268.
(9) Thallapally, P. K.; Tian, J.; Radha Kishan, M.; Fernandez, C. A.; Dalgarno, S. J.; McGrail, P. B.; Warren, J. E.; Atwood, J. L. Flexible (Breathing) Interpenetrated Metal-Organic Frameworks for CO2 Separation Applications. *J. Am. Chem. Soc.* **2008**, *130* (50), 16842.
(10) Pham, T. D.; Hudson, M. R.; Brown, C. M.; Lobo, R. F. Molecular Basis for the High CO2 Adsorption Capacity of Chabazite Zeolites. *ChemSusChem* **2014**, *7* (11), 3031−3038.
(11) Zeng, Y. F.; Zou, R. Q.; Zhao, Y. L. Covalent Organic Frameworks for CO2 Capture. *Adv. Mater.* **2016**, *28* (15), 2855−2873.
(12) Das, A. K.; Vemuri, R. S.; Kutnyakov, I.; McGrail, B. P.; Motkuri, R. K. An Efficient Synthesis Strategy for Metal-Organic Frameworks: Dry-Gel Synthesis of MOF-74 Framework with High Yield and Improved Performance. *Sci. Rep.* **2016**, *6*, 28050.
(13) Thakkar, H.; Eastman, S.; Hajari, A.; Rownaghi, A. A.; Knox, J. C.; Rezaei, F. 3D-Printed Zeolite Monoliths for CO2 Removal from Enclosed Environments. *ACS Appl. Mater. Interfaces* **2016**, *8* (41), 27753−27761.
(14) Hudson, M. R.; Queen, W. L.; Mason, J. A.; Fickel, D. W.; Lobo, R. F.; Brown, C. M. Unconventional, Highly Selective CO2 Adsorption in Zeolite SSZ-13. *J. Am. Chem. Soc.* **2012**, *134* (4), 1970−1973.
(15) Oleksiak, M. D.; Ghorbanpour, A.; Conato, M. T.; McGrail, B. P.; Grabow, L. C.; Motkuri, R. K.; Rimer, J. D. Synthesis Strategies for Ultrastable Zeolite GIS Polymorphs as Sorbents for Selective Separations. *Chem. - Eur. J.* **2016**, *22* (45), 16078−16088.
(16) Luo, Y.; Funke, H. H.; Falconer, J. L.; Noble, R. D. Adsorption of CO2, CH4, C3H8, and H2O in SSZ-13, SAPO-34, and T-Type Zeolites. *Ind. Eng. Chem. Res.* **2016**, *55* (36), 9749−9757.
(17) Pham, T. D.; Liu, Q. L.; Lobo, R. F. Carbon Dioxide and Nitrogen Adsorption on Cation-Exchanged SSZ-13 Zeolites. *Langmuir* **2013**, *29* (2), 832−839.
(18) Prodinger, S.; Vemuri, R. S.; Varga, T.; McGrail, B. P.; Motkuri, R. K.; Derewinski, M. A. Impact of chabazite SSZ-13 textural properties and chemical composition on CO2 adsorption applications. *New J. Chem.* **2016**, *40* (5), 4375−4385.
(19) Shang, J.; Li, G.; Singh, R.; Gu, Q. F.; Nairn, K. M.; Bastow, T. J.; Medhekar, N.; Doherty, C. M.; Hill, A. J.; Liu, J. Z.; Webley, P. A. Discriminative Separation of Gases by a "Molecular Trapdoor" Mechanism in Chabazite Zeolites. *J. Am. Chem. Soc.* **2012**, *134* (46), 19246−19253.

DOI: 10.1021/acsami.8b03848
ACS Appl. Mater. Interfaces 2018, 10, 14287−14291

(20) Civalleri, B.; Ferrari, A. M.; Llunell, M.; Orlando, R.; Merawa, M.; Ugliengo, P. Cation selectivity in alkali-exchanged chabazite: An ab initio periodic study. *Chem. Mater.* **2003**, *15* (21), 3996−4004.
(21) Bae, T. H.; Hudson, M. R.; Mason, J. A.; Queen, W. L.; Dutton, J. J.; Sumida, K.; Micklash, K. J.; Kaye, S. S.; Brown, C. M.; Long, J. R. Evaluation of cation-exchanged zeolite adsorbents for post-combustion carbon dioxide capture. *Energy Environ. Sci.* **2013**, *6* (1), 128−138.
(22) Tang, J. D.; Zhou, Y. P.; Su, W.; Liu, X. W.; Sun, Y. Synthesis of Zeolite SSZ-13 for N-2 and CO2 Separation. *Adsorpt. Sci. Technol.* **2013**, *31* (6), 549−558.
(23) Hong, S. H.; Jang, M. S.; Cho, S. J.; Ahn, W. S. Chabazite and zeolite 13X for CO2 capture under high pressure and moderate temperature conditions. *Chem. Commun.* **2014**, *50* (38), 4927−4930.
(24) Miyamoto, M.; Fujioka, Y.; Yogo, K. Pure silica CHA type zeolite for CO2 separation using pressure swing adsorption at high pressure. *J. Mater. Chem.* **2012**, *22* (38), 20186−20189.
(25) Prodinger, S.; Derewinski, M. A.; Wang, Y. L.; Washton, N. M.; Walter, E. D.; Szanyi, J.; Gao, F.; Wang, Y.; Peden, C. H. F. Sub-micron Cu/SSZ-13: Synthesis and application as selective catalytic reduction (SCR) catalysts. *Appl. Catal., B* **2017**, *201*, 461−469.
(26) Smith, L. J.; Eckert, H.; Cheetham, A. K. Potassium cation effects on site preferences in the mixed cation zeolite Li,Na-chabazite. *Chem. Mater.* **2001**, *13* (2), 385−391.
(27) Oschatz, M.; Antonietti, M. A search for selectivity to enable CO2 capture with porous adsorbents. *Energy Environ. Sci.* **2018**, *11* (1), 57−70.
(28) Krishna, R. The Maxwell-Stefan description of mixture diffusion in nanoporous crystalline materials. *Microporous Mesoporous Mater.* **2014**, *185*, 30−50.
(29) Lavalley, J. C. Infrared spectrometric studies of the surface basicity of metal oxides and zeolites using adsorbed probe molecules. *Catal. Today* **1996**, *27* (3−4), 377−401.
(30) Ridha, F. N.; Yang, Y. X.; Webley, P. A. Adsorption characteristics of a fully exchanged potassium chabazite zeolite prepared from decomposition of zeolite Y. *Microporous Mesoporous Mater.* **2009**, *117* (1−2), 497−507.
(31) Krishna, R. Screening metal-organic frameworks for mixture separations in fixed-bed adsorbers using a combined selectivity/capacity metric. *RSC Adv.* **2017**, *7* (57), 35724−35737.

DOI: 10.1021/acsami.8b03848
ACS Appl. Mater. Interfaces 2018, 10, 14287−14291

Supporting Information

Dynamic Adsorption of CO_2/N_2 on Cation-Exchanged Chabazite SSZ-13: A Breakthrough Analysis

Jamey K. Bower,[†,¥] Dushyant Barpaga,[‡] Sebastian Prodinger,[†] Rajamani Krishna,[§] H. Todd Schaef,[†] B. Peter McGrail,[‡] Miroslaw A. Derewinski,[†,] and Radha Kishan Motkuri [†,*]*

[†] Physical and Computational Sciences Division, Pacific Northwest National Laboratory (PNNL), Richland, Washington 99352, USA

[‡] Energy and Environment Directorate, Pacific Northwest National Laboratory (PNNL), Richland, WA 99352, USA

[¥] Department of Chemistry and Biochemistry, The Ohio State University, Columbus, OH 43210

[§] Van‘t Hoff Institute for Molecular Sciences, University of Amsterdam, Science Park 904, 1098 XH Amsterdam, The Netherlands

*To whom correspondence should be addressed. Tel: +1 (509) 371-6484; +1 (509) 375-3856
E-mail: Radhakishan.Motkuri@pnnl.gov; Miroslaw.Derewinski@pnnl.gov

Table of Contents

General procedures, materials, and instrumentations:

Experimental Methods

Synthesis of these high-silica-containing-zeolites requires the use of templating organic molecules, in this case trimethyl-adamantyl ammonium hydroxide (TMAda-OH). The positively charged $TMAda^+$ molecule also fulfills a further function in partially balancing the negative charge of the zeolite framework induced by the incorporation of Al^{3+} into a Si^{4+} oxide network. Besides ammonium cations, inorganic alkali cations, introduced during the synthesis or by post-synthetic ionic exchange procedures, also compensate part of the framework charge. The smaller size of these alkali cations, enables the successful synthesis of SSZ-13 zeolites with low Si/Al ratios as well as affecting the Al-siting.[1,2]

Synthesis of materials

As-made. SSZ-13 was synthesized according to the procedure described by Prodinger et al[3]. In short, a gel with the composition $20TMAdaOH:10Na_2O:8.3Al_2O_3:100SiO_2:4400H_2O$ was prepared. NaOH (Aldrich) was initially dissolved in H_2O followed by the sequential addition of $Al(OH)_3$ (54% Al_2O_3, Aldrich) and N,N,N-trimethyladamantyl-ammonium hydroxide (24.8 wt% in H_2O, Sachem Zeogen 2825). After the stirred solution became clear, fumed silica (0.007 μm average particle size, Aldrich) was slowly added. The gel was aged at room temperature for 24 h prior to being placed in a Teflon-lined autoclave, placed on a stir plate (160 rpm), heated to 160 °C and kept under these conditions for 4 days. Upon completion of the synthesis the suspension

was centrifuged and the solid residue was washed with deionized water to neutral pH before being dried overnight at 80 °C.

Calcined (Na/H-form). To remove the organic structure directing agent, TMAdaOH, the zeolite was calcined first at 200 °C in synthetic air for 1 hour followed by 8 hours at 550 °C with a heating rate of 1 °C min^{-1}. The obtained calcined zeolite, denoted as Na/H-form, had a Si/Al of 5 determined with atomic absorption spectroscopy.[3]

Ionic exchange. The Na/H-form was first exchanged to the NH_4-form of SSZ-13. First, 0.8 g of Na/H-SSZ-13 was immersed in 400 mL of a stirred 0.1 M $NH_4NO_{3(aq)}$ solution at 80 °C and kept overnight. The suspension was then separated by centrifuge and the solid residue was washed 3 times with 250 mL of deionized water until pH 7 was reached and then dried at 80 °C. To obtain Li^+, K^+ and Na^+ exchanged forms of SSZ-13, two different ionic exchange procedures were employed. The first involved dispersing 0.4 g of NH_4-SSZ-13 in 400 mL of aqueous 0.1 M $NaNO_3$. The suspension was stirred overnight at 80 °C and then separated by centrifuge with the solid residue being washed twice with 250 mL of deionized water until pH 7 was reached, followed by drying at 80 °C. The sample was hereafter known as 1Na-SSZ-13.

Additionally, an ionic exchange procedure reported by Gao et al.[4] was utilized by immersing 0.4 g of NH_4-SSZ-13 in 400 mL of 0.1 M $NaNO_3$, $LiNO_3$ or KNO_3 solution. This solution was stirred at 80 °C for 1 hour and then separated before re-dispersing the solid residue in fresh solution and repeating the exchange at 80 °C for 1 hour. After completing the ionic exchange the solid residue was washed twice with 250 mL deionized water and then dried at 80 °C.

The samples obtained by these procedures were denoted by the number of ionic exchange steps, e.g. 1Na-SSZ-13, 2Na-SSZ-13, 2Li-SSZ-13, etc.

X-ray diffraction (XRD)

A Rigaku Mini Flex II benchtop X-ray diffractometer using a Cu-Ka radiation of 0.154056 nm (30 kV and 15 mA) was used to obtain diffractograms of the zeolite samples. The samples were place in a powder sample holder and scanned from 5 to 65 ° 2θ with a step size of 2°/min under ambient conditions.

N_2-physisorption

N_2 adsorption at 77K was performed on an ASAP 2020 Micromeritics Porosimeter to calculate the surface area and pore volumes of all samples. The samples were activated prior to measurement by heating to 300° C and maintaining this temperature for 6 h under vacuum. The apparent surface area was determined using the BET method from the linear region of the isotherm yielding a positive C-constant as reported by Rouquerol et al.[5] Single point adsorption at approximately P/P_0=0.99 was used to determine the total pore volume of each material. The micropore volume and corresponding pore size distribution was determined using NL-DFT kernels for N_2 in cylindrical pores on oxide surfaces as provided by the Micromeritics suite.

TGA-MS

Thermogravimetric analysis paired with mass spectrometry (TGA-MS) was performed on the materials to measure the percent of mass lost after activation/regeneration of the material. The

instrument used was a Netzsch Instruments TG-209 F1 under a program of 5K/min ramp rate to a maximum temperature of 500°C with N_2 flow (20 mL/min). The mass spectrometric analysis was performed on a QMS 403 C Aeolos by Netzsch Instruments, while recording evolution of H_2O (18 m/z). The amount of sample mass used for an experiment was typically between 9.0 and 11.0 mg.

Thermogravimetric analysis (Figure S4) showed a loss of mass on the order of roughly 15% for each of the materials due to desorption of water and extraneous gas molecules residing within the pores of the materials. This desorption simulates the regeneration of the material performed in between characterization trials. This corrected mass after weight loss was utilized in the calculation of capacity measurements.

Elemental Analysis (ICP-MS)

The elemental composition was determined using ICP-MS after completely digesting the aluminosilicate samples in a HNO_3/HF mixture and complexation of unreacted fluoride anions with H_3BO_3.

Equilibrium Adsorption Measurements

CO_2 and N_2 adsorption isotherms

Equilibrium CO_2 and N_2 adsorption isotherms were collected using an Autosorb iQ2 Quantachrome automated gas sorption analyzer. Each isotherm was measured with a volumetric dosing method from ~2.5-101.3 kPa at 15, 25, and 35°C for CO_2 and 15, 20, 25°C for N_2. The temperature was maintained using a water bath. Prior to analysis, each sample was outgassed for 12 hours at 110°C under vacuum.

The resulting unary isotherm was fit using the 1-site Langmuir-Freundlich model (eq. 1) for CO_2 and the 1-site Langmuir model (eq. 2) for N_2 with the fitted parameters being reported in Table S2 and Table S3.

$$q = q_{sat}\frac{bp^v}{1+bp^v} \quad (1)$$

$$q = q_{sat}\frac{bp}{1+bp} \quad (2)$$

Heats of adsorption

The heats of adsorption were calculated using the fitted parameters along with the Clausius-Clapeyron equation.

IAST calculations for mixture adsorption equilibrium

SSZ-13 has CHA zeolite topology. The cages of volume 316 $Å^3$ are separated by 3.8 Å × 4.2 Å 8-ring windows, as shown in Figure S1.

Two commonly used metrics for comparing and evaluating the separation performance of adsorbents are selectivity and capacity. For separation of a binary mixture of components A (CO_2) and B (N_2), the adsorption selectivity, S_{ads}, is defined by

$$S_{ads} = \frac{q_A/q_B}{y_A/y_B} \quad (3)$$

where the q_A, and q_B represent the molar loadings within the adsorbent that is in equilibrium with a bulk gas phase mixture with mole fractions y_A, and $y_B = 1 - y_A$. In this work, we analyze 15/85 CO_2/N_2 mixtures, and $y_A = 0.15$ and $y_B = 0.85$. The molar loadings, also called gravimetric uptake capacities, are usually expressed with the units mol kg^{-1}. The volumetric uptake capacities, are

$$Q_A = \rho q_A \; ; Q_B = \rho q_B \quad (4)$$

where ρ is the crystal framework density of the adsorbent, expressed say in units of kg m^{-3}, or kg L^{-1}. The framework densities for the five SSZ-13 adsorbents are provided in Table S4. The uptake capacities are calculated using unary isotherm fits, along with the Ideal Adsorbed Solution Theory (IAST) of Myers and Prausnitz[6] for adsorption equilibrium. For 15/85 CO_2/N_2 mixtures at 298 K, and 100 kPa, IAST calculations of the adsorption selectivity versus the volumetric CO_2 uptake for Na/H, 1Na, 2Na, 2K, and 2Li can be computed. The selectivity values of two benchmark adsorbents NiMOF-74, and 13X zeolite are also included for comparison. Their structural and isotherm data are provided in Tables S5, S6, and S7.

Dynamic Breakthrough Adsorption Measurements

A flow-through system for gas breakthrough experiments was assembled, a schematic of which is shown in Scheme 1. The pure carrier gas, in this case helium, flowed from the gas cylinder through the manifold at approximately 101 kPa. Initially, the flow-through column (internal

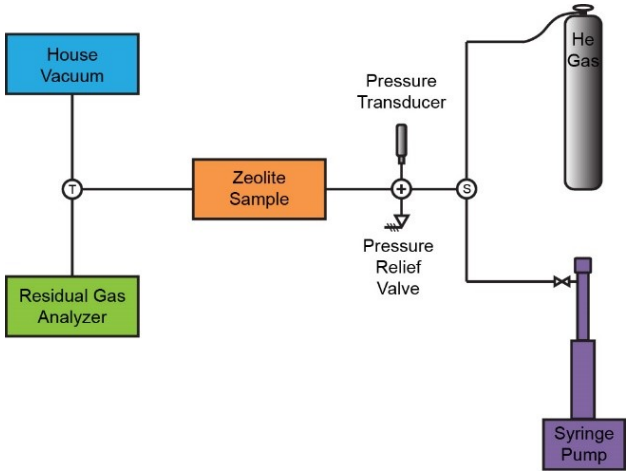

Scheme S1: A schematic representation of the experimental dynamic adsorption apparatus is shown.

diameter 0.18 in) capped with glass wool containing approximately between 100 and 250 mg of sample was opened to the flow of helium purge gas. After passing through the column, the

majority of the helium was taken up by the vacuum, while a small aliquot of the total volume was extracted by the Stanford Research Systems residual gas analyzer 200 (RGA) attached to a Varian Turbo V-70 vacuum pump in line with an Edwards XDS 10 dry roughing pump, which measures the partial pressure of gases that compose the effluent. At this juncture, the RGA trial was initiated and the readings from the RGA were allowed to stabilize for several minutes while on helium flow. Once the system had stabilized, the chosen gas mixture was introduced to the system by turning on the pump and manually switching from helium to the syringe pump. A calibrated mixture of 85% nitrogen and 15% carbon dioxide (OXARC Inc.) was used. The composition of CO_2 and N_2 in flue gas will vary based on the level of moisture, oxygen content, and harsher toxic gases like SO_2 and NO_x. However, in order to focus on the interaction between the cation exchanged materials and limited guest molecules for our experiments, a simplified mixture was chosen as a representative of simulated conditions. Prior to the experiment, the syringe pump was pressurized to approximately atmospheric pressure (ca. 101 kPa), and set to a constant flow rate of 1 mL/min. In order to maintain constant pressure in the manifold at the designated flow rate, a valve was in place that regulates the amount of gas being vacuumed out of the system after having passed through the column. This pressure was measured with a calibrated pressure transducer (Omega Engineering) and the components of the setup were connected with PEEK polymer tubing (0.030 in internal diameter). Experiments were run until full breakthrough of the gas mixture was achieved in the RGA, signaled by flat lines in the readout.

Prior to the first run, the material was activated at 150 °C for approximately 15 hours in order to remove any guest molecules remaining residually in the framework, such as water or oxygen. Custom aluminum blocks were crafted to fit around the flow-through column, which were fastened with heating tape and clamped into place. The heater was plugged into an Extech Process PID

controller that connects to a thermocouple used to measure the real-time temperature of the aluminum blocks. During the activation/regeneration process, the column was open to the vacuum side of the system and a helium stream that flowed through.

Capacity Calculation Methodology

Breakthrough measurements were conducted with the 85% N_2 and 15% CO_2 mixture at room temperature in order to demonstrate how the SSZ-13 zeolites would behave under conditions similar to post-combustion flue gas. Initially, no CO_2 is detected at the outlet. As adsorption sites begin to saturate, small amounts of CO_2 begin to pass through the material without being adsorbed, the RGA detects increasing amounts of CO_2, generating a breakthrough curve until the partial pressure of CO_2 reaches its maximum at the composition of the complete gas mixture being passed through the material. The CO_2 capacity (mol/kg) of the material was calculated by the equation

$$n = \frac{F}{m}\int_0^{\infty}(C_0 - C)\,dt \qquad (5)$$

where C_0 is the adsorbate feed concentration of, C is the concentration of the adsorbate in the effluent at time t. The integral is multiplied by a factor that is the quotient of the feed concentration flowrate F and the mass of the sample in the adsorbent bed, m. This calculation integrates the area above the breakthrough curve, which represents the quantity of CO_2 adsorbed. For simplification, in this model, the concentration of gas at any given time is assumed to be in the adsorbed phase rather than simply occupying pore space without interacting with framework (bulk phase).

The error in capacity calculation was derived from run to run for the same batch of material. Deviations range from ±5-10% of the average capacity determined from a minimum of 3 reproduced runs for each material with regenerated adsorbent.

Simulation of separation in fixed bed adsorbers

As a means of enhancing CO_2 separation efforts, one can also consider the objective of purifying N_2, leaving the residual stream, CO_2 enriched. Thus, we can compare the adsorbents on their ability to produce pure nitrogen. The maximum achievable productivity of pure N_2 is realized when both intracrystalline diffusion and axial dispersion effects are completely absent and the concentrations "fronts" of the fluid mixture traverse the fixed bed in the form of shock waves.[7] For a binary mixture with mole fractions y_A and $y_b = 1 - y_A$ in the feed mixture, the maximum achievable productivity, ΔQ, called the separation potential can be calculated using the shock-wave model; the result is[7]:

$$\Delta Q = \left(Q_{CO2} \frac{y_{N2}}{1-y_{N2}} - Q_{N2} \right) \qquad (6)$$

The physical significance of ΔQ, conveniently expressed in the units of mol per L of adsorbent, is that it represents the maximum amount of pure component N_2 (less strongly adsorbed component) that can be recovered during the adsorption phase of fixed bed separations. The value of ΔQ can be determined from IAST calculations.

In practice, the productivities will be lower than the values calculated from equation (6) due to the distended nature of breakthroughs due to a variety of reasons such as intra-crystalline diffusion, and finite values of selectivities. For a proper evaluation of the separation performance of different adsorbents, we performed transient breakthrough simulations, where the methodology used in the

simulations is the same as that described in detail in previous works.[7-9] A brief summary is provided hereunder.

We neglect axial dispersion effects and consider plug flow of an n-component gas mixture through a fixed bed adsorber maintained under isothermal, isobaric, conditions; see Figure S6. The molar concentrations of the constituent species in the bulk fluid phase vary with position z along the bed, and time, t. At any position z in the fixed bed, and time t, the molar loadings in the adsorbed phase within the pores, varies along the radius of the particle, r. The molar concentrations in the gas phase at any position and instant of time are obtained by solving the following set of partial differential equations for each of the species i in the gas mixture.[10]

$$\frac{\partial c_i(t,z)}{\partial t} + \frac{\partial (v(t,z)c_i(t,z))}{\partial z} + \frac{(1-\varepsilon)}{\varepsilon}\rho\frac{\partial \bar{q}_i(t,z)}{\partial t} = 0; \quad i = 1,2,\ldots n \qquad (7)$$

In equation (7), t is the time, z is the distance along the adsorber, ρ is the framework density, ε is the bed voidage, v is the interstitial gas velocity, and $\bar{q}_i(t,z)$ is the spatially averaged molar loading within the crystallites of radius r_c, monitored at position z, and at time t. The time t = 0, corresponds to the time at which the feed mixture is injected at the inlet to the fixed bed. Prior to injection of the feed, it is assumed that an inert, non-adsorbing, gas flows through the fixed bed.

At any time, t, during the transient approach to thermodynamic equilibrium, the spatially averaged molar loading within the crystallite r_c is obtained by integration of the radial loading profile:

$$\bar{q}_i(t) = \frac{3}{r_c^3}\int_0^{r_c} q_i(r,t)r^2 dr \qquad (8)$$

For transient unary uptake within a crystal at any position and time with the fixed bed, the radial distribution of molar loadings, q_i, within a spherical crystallite, of radius r_c, is obtained from a solution of a set of differential equations describing the uptake

$$\frac{\partial q_i(r,t)}{\partial t} = -\frac{1}{\rho}\frac{1}{r^2}\frac{\partial}{\partial r}(r^2 N_i) \tag{9}$$

The molar flux N_i of component i may be described by the simplified version of the Maxwell-Stefan equations in which both correlation effects and thermodynamic coupling effects are considered to be of negligible importance[8]

$$N_i = -\rho Đ_i \frac{\partial q_i}{\partial r} \tag{10}$$

Summing equation (8) over all n species in the mixture allows calculation of the total average molar loading of the mixture within the crystalline:

$$\bar{q_t}(t,z) = \sum_{i=1}^{n} \bar{q_i}(t,z) \tag{11}$$

The interstitial gas velocity is related to the superficial gas velocity by:

$$v = \frac{u}{\varepsilon} \tag{12}$$

The molar loadings at the outer surface of the crystallites, i.e. at $r = r_c$, are calculated on the basis of adsorption equilibrium with the bulk gas phase partial pressures p_i at that position z and time t. The adsorption equilibrium can be calculated on the basis of the IAST description of mixture adsorption equilibrium.

The adsorber bed that is operated under isothermal, isobaric conditions is assumed to be initially free of adsorbates, i.e. we have the initial condition:

$$t = 0; \quad q_i(0,z) = 0 \tag{13}$$

Equation (13) is relevant to the operation of the transient breakthrough experiments on a laboratory scale, but is not truly reflective of industrial operations.

At time, t = 0, the inlet to the adsorber, z = 0, is subjected to a step input of the n-component gas mixture and this step input is maintained till the end of the adsorption cycle when steady state conditions are reached.

$$t \geq 0; \quad p_i(0,t) = p_{i0}; \quad u(0,t) = u_0 \tag{14}$$

where $u_0 = v_0\varepsilon$ is the superficial gas velocity at the inlet to the adsorber.

The experimental data for Na/H, 1Na, 2Na, 2K, and 2Li adsorbents (cf. Figure S7a) show distended characteristics for CO_2 breakthroughs. This indicates that intra-crystalline diffusion effects are non-negligible. The parameter $\frac{Đ_i}{r_c^2}$ quantifies the intra-crystalline diffusion limitations.

We first performed transient breakthrough simulations under the precise conditions of the breakthrough experiments for the five SSZ-13 experiments in order to determine the parameter values $\frac{Đ_i}{r_c^2}$. Figures S7(b,c,d,e,f) present comparisons of the experimental data on CO_2 breakthroughs for (b) Na/H, (c) 1Na, (d) 2Na, (e) 2K, and (f) 2Li adsorbents with transient breakthrough simulations taking $\frac{Đ_{CO2}}{r_c^2} = 2x10^{-4}s^{-1}$, and $\frac{Đ_{N2}}{r_c^2} = 2x10^{-3}s^{-1}$. These fitted diffusivity values capture the essential characteristics of the experimental breakthroughs; the fitted values were used for purposes of comparative evaluations.

For the benchmark adsorbents Ni-MOF-74 and 13X zeolite, the value of $\frac{Đ_i}{r_c^2}$ is large enough to ensure that intra-crystalline gradients are absent and the entire crystallite particle can be considered

to be in thermodynamic equilibrium with the surrounding bulk gas phase at that time t, and position z of the adsorber:

$$\overline{q_t}(t,z) = q_i(t,z) \tag{15}$$

Comparison of SSZ-13 with benchmark adsorbents

For comparing the separations with SSZ-13 with benchmark adsorbents NiMOF-74 and 13X zeolite, we choose the following dimensions for the fixed bed adsorber: adsorber length, L = 0.3m; cross-sectional area, A = 1 m^2; superficial gas velocity in the bed, u_0 = 0.04 m s^{-1}; voidage of the packed bed, ε = 0.4. In these breakthrough simulations we use the same volume of adsorbent in the breakthrough apparatus, i.e. (1 - ε) A L = 0.18 m^3 = 180 L.

For presenting the breakthrough simulation results, we use the dimensionless time, $\tau = \frac{tu}{L\varepsilon}$, obtained by dividing the actual time, t, by the characteristic time, $\frac{L\varepsilon}{u}$, where L is the length of the adsorber, u is the superficial fluid velocity, and ε is the bed voidage.[11] As illustration, Figure S8 presents the transient breakthrough simulations for 15/85 CO_2/N_2 mixtures at 298 K, and 100 kPa in a fixed bed packed with 2K-SSZ-13. During the time interval Δτ, as indicated in Figure S8, pure N_2 can be recovered. We arbitrarily demand a purity of 99.95% for N_2. From a material balance on the adsorber, we can determine the productivity of 99.95% pure N_2 from the transient breakthrough simulations.

The separation potential $\Delta Q = Q_{CO2}\frac{0.85}{0.15} - Q_{N2}$ can also be computed and evaluated against the productivity to evaluate the separation performance of the adsorbents.

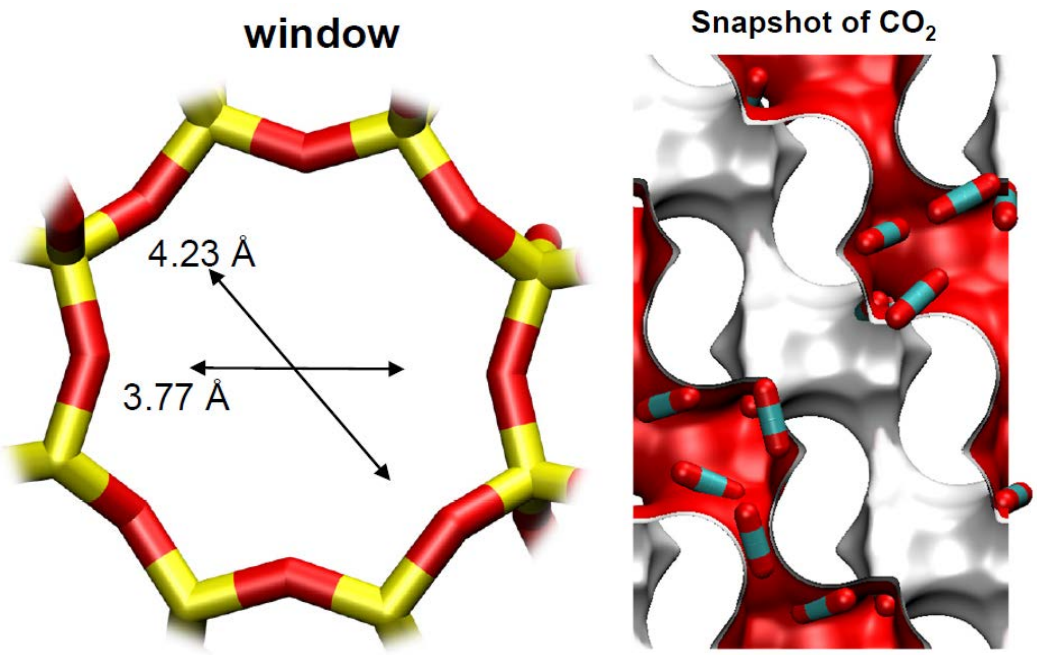
window
4.23 Å
3.77 Å
Snapshot of CO_2

Figure S1. Pore landscape and structural details of CHA zeolite framework consisting of three double six-membered-ring units.[3]

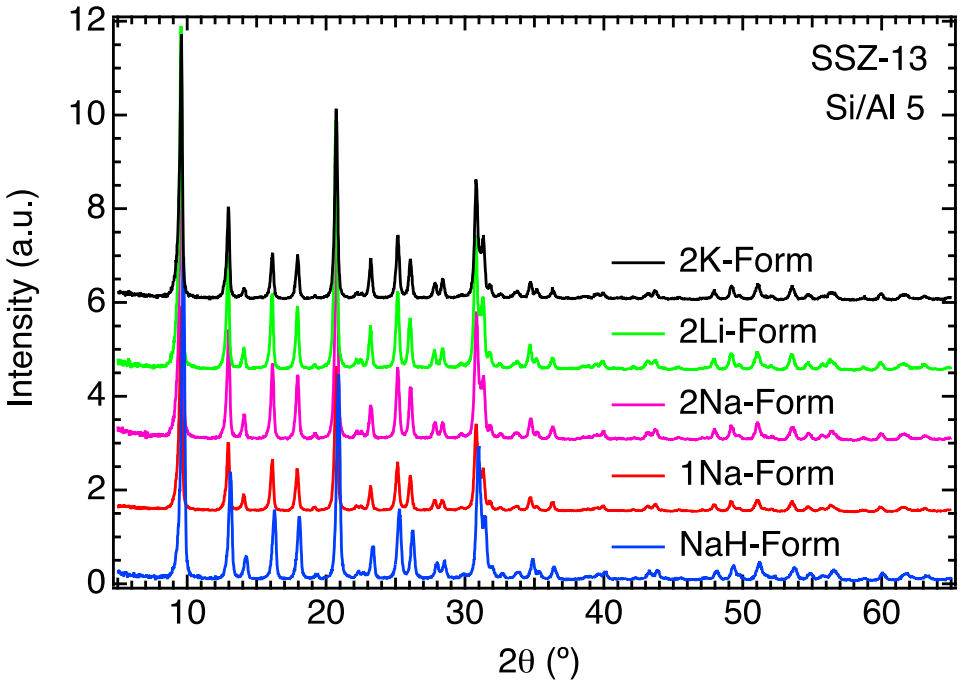

Figure S2. Powder X-ray diffractograms (PXRD) showing the various exchanged forms of SSZ-13. Patterns matching the CHA framework structure are observed in all cases. Individual samples are denoted in the legend.

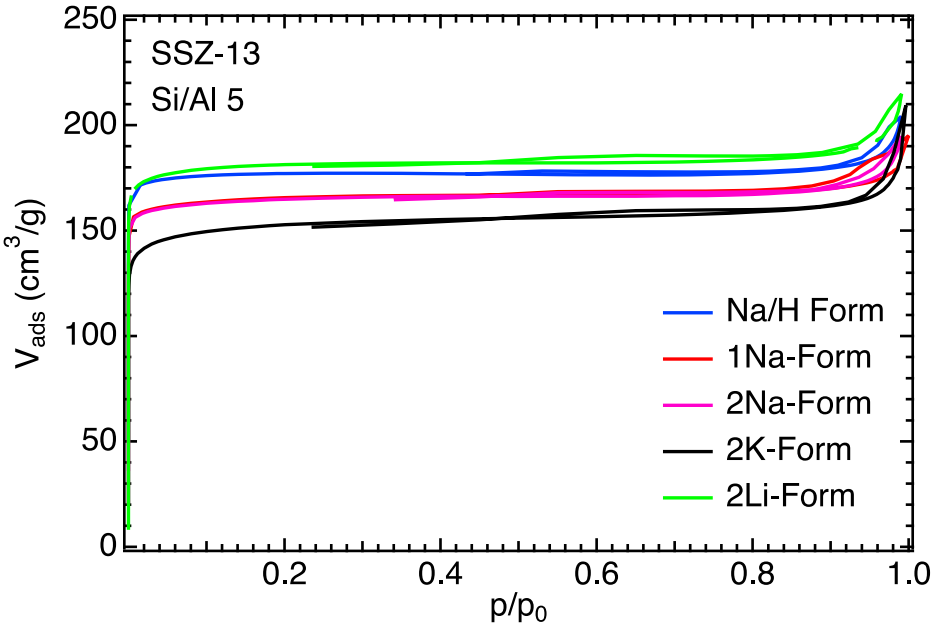

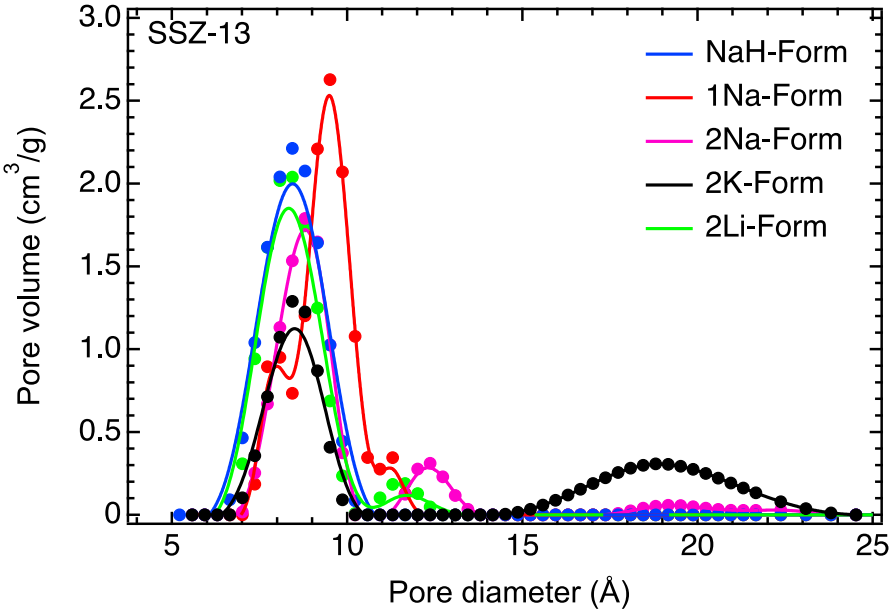

Figure S3. N_2 equilibrium isotherms at 77K and corresponding pore size distributions as determined with NL-DFT models for the alkali exchanged SSZ-13 materials.

Table S1. Cation exchange degrees as determined by elemental analysis and pore geometries calculated from N_2 isotherms at 77K.

Material	**Cation/Al**	**BET (m^2/g)**	**Micropore volume (cm^3/g)**
Na/H-SSZ-13	0.6	735	0.26
1Na-SSZ-13	0.7	680	0.25
2Na-SSZ-13	0.78	675	0.25
2K-SSZ-13	0.78	600	0.19
2Li-SSZ-13	0.83	735	0.27

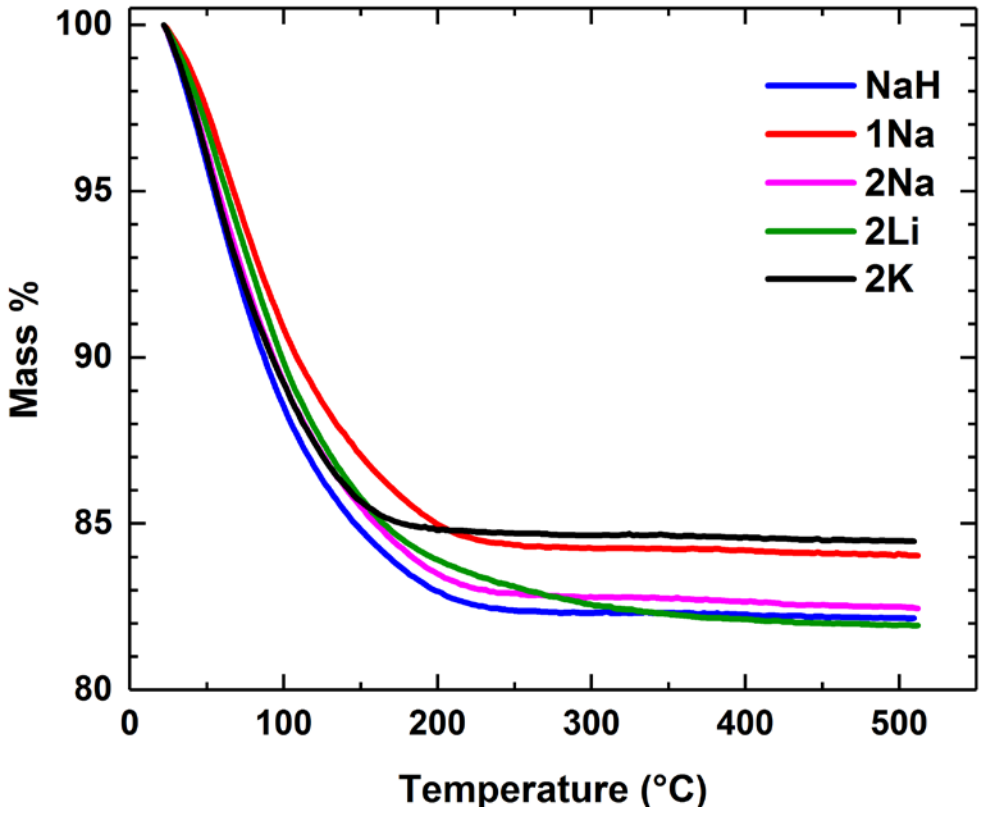

Figure S4. TGA-MS for the synthesized SSZ-13 samples.

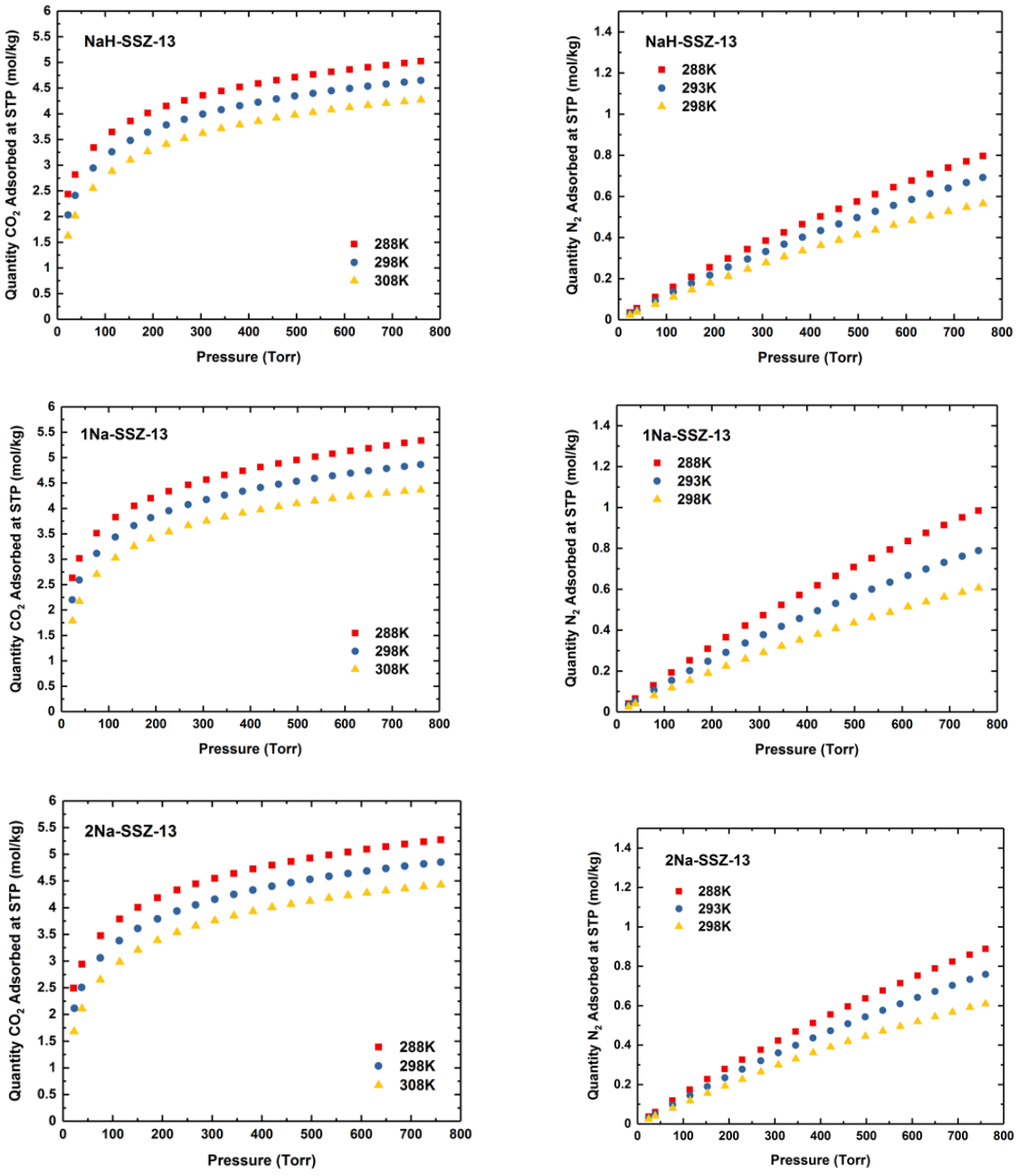

Figure S5. Equilibrium CO_2 and N_2 adsorption isotherms for Na/H, 1Na and 2Na-SSZ-13 samples at different temperatures.

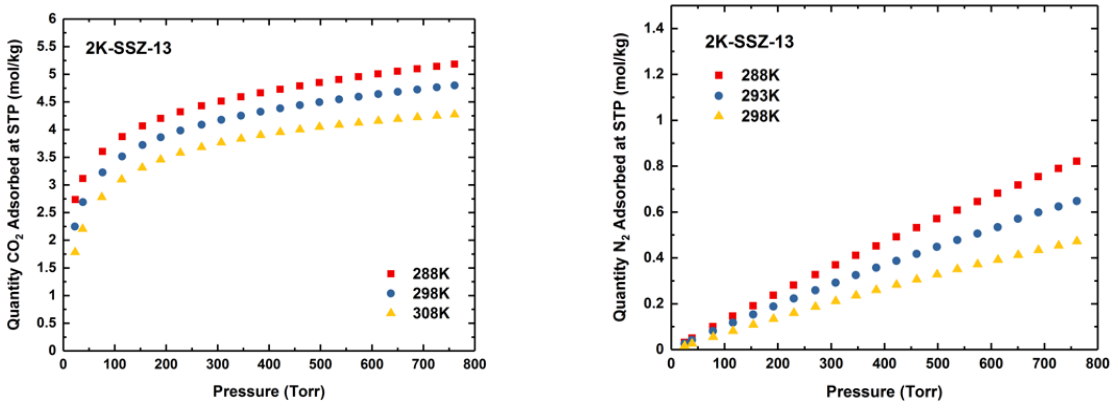

Figure S6. Equilibrium CO_2 and N_2 adsorption isotherms for 2K-SSZ-13 samples at different temperatures.

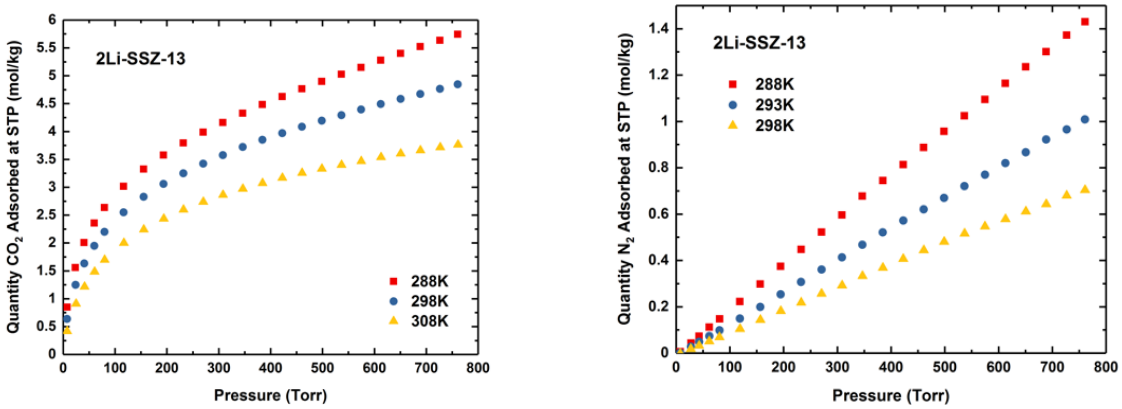

Figure S7. Equilibrium CO_2 and N_2 adsorption isotherms for 2Li-SSZ-13 samples at different temperatures.

Table S2. Heat of adsorption for SSZ-13 samples as calculated using the Clausius Clapyeron equation after fitting equilibrium isotherms at different temperatures to the 1-site Langmuir-Freundlich adsorption model (eq. 1). *Qst values were averaged over the range of uptake amounts given the negligible difference in heat evolved as a function of loading.

Chabazite samples	**Heat of Adsorption* (kJ/mol)**
Na/H-SSZ-13	41.0
1Na-SSZ-13	41.5
2Na-SSZ-13	41.6
2K-SSZ-13	45.2
2Li-SSZ-13	39.6

Table S3. Fitted parameters derived from the 1-site Langmuir-Freundlich model using experimental, unary, equilibrium CO_2 adsorption isotherms for each SSZ-13 sample measured at 298K.

	q_{sat} mol kg^{-1}	b $Pa^{-\nu}$	ν dimensionless
Na/H	6.6	0.0105639	0.47
1Na	7	0.0139914	0.44
2Na	8	0.0154877	0.4
2K	7.1	0.0206957	0.4
2Li	10	0.0020394	0.53

Table S4. Fitted parameters derived from the 1-site Langmuir model using experimental, unary, equilibrium N_2 adsorption isotherms for each SSZ-13 sample measured at 298K.

	q_{sat} mol kg^{-1}	b Pa^{-1}
Na/H	2.2	3.5071E-06
1Na	2.2	3.7847E-06
2Na	2.6	3.1337E-06
2K	6.6	7.8857E-07
2Li	7	1.0941E-06

Table S5. Framework densities of the SSZ-13 adsorbent samples.

	Framework density kg m^{-3}
Na/H	1535.9
1Na	1543.2
2Na	1548.6
2K	1591.3
2Li	1507.1

Table S6. Structural data for Ni-MOF-74 and 13X zeolite.

Sorbent	**Surface area (m^2/g)**	**Pore volume (cm^3/g)**	**Framework density (kg/m^3)**
Ni-MOF-74	1532	0.582	1194
13X zeolite	950	0.280	1421
NiMOF-74 = (Ni_2(dobdc) where dobdc = (dobdc = 1,4-dioxido-2,5-benzenedicarboxylate)). This MOF consists of one-dimensional hexagonal-shaped channels with free internal diameter of ca. 11 Å. The 13 X zeolite, has FAU topology. The FAU topology consists of 785.7 $Å^3$ size cages separated by 7.4 Å size windows. Cage size is calculated on the basis of the equivalent sphere volume.			

Table S7. 1-site Langmuir-Freundlich parameters for unary CO_2 and N_2 isotherms at 298 K in Ni-MOF-74.

	q_{sat} **(mol/kg)**	b **(Pa$^{-\nu}$)**	ν dimensionless
CO_2	9.4	9.0242E-04	0.66
N_2	9.4	1.1911E-03	0.44

Table S8. Fitted parameters derived from dual-site Langmuir model using CO_2 and N_2 adsorption isotherms reported by Belmabkhour et al.[13] and Cavenati et al.[14] for 13X zeolite measured at 298K. The fits were performed after converting the excess data to absolute loadings.

	$q_{A,sat}$ mol kg^{-1}	b_A Pa^{-1}	E_A kJ mol^{-1}	$q_{B,sat}$ mol kg^{-1}	b_B Pa^{-1}	E_B kJ mol^{-1}
CO_2	3.5	3.6449E-13	35	5.2	6.0389E-11	35
N_2	3	4.0754E-09	13	6	4.6812E-10	13

Dual-site Langmuir model: $$q = q_{A,sat}\frac{b_A p}{1+b_A p} + q_{B,sat}\frac{b_B p}{1+b_B p},$$

with T-dependent b_A and b_B: $$b_A = b_{A0}\exp\left(\frac{E_A}{RT}\right); \quad b_B = b_{B0}\exp\left(\frac{E_B}{RT}\right)$$

Table S9. Bulk CO_2 capacities obtained by integrating the breakthrough adsorption profiles obtained using a CO_2/N_2 gas mixture flowing through a packed bed of sample at 298K and 1 bar. The calculations were performed using equation (5).

Sample	CO_2 Capacity (mmol/g)
NaH	1.44
1Na	2.07
2Na	2.04
2K	1.79
2Li	1.88

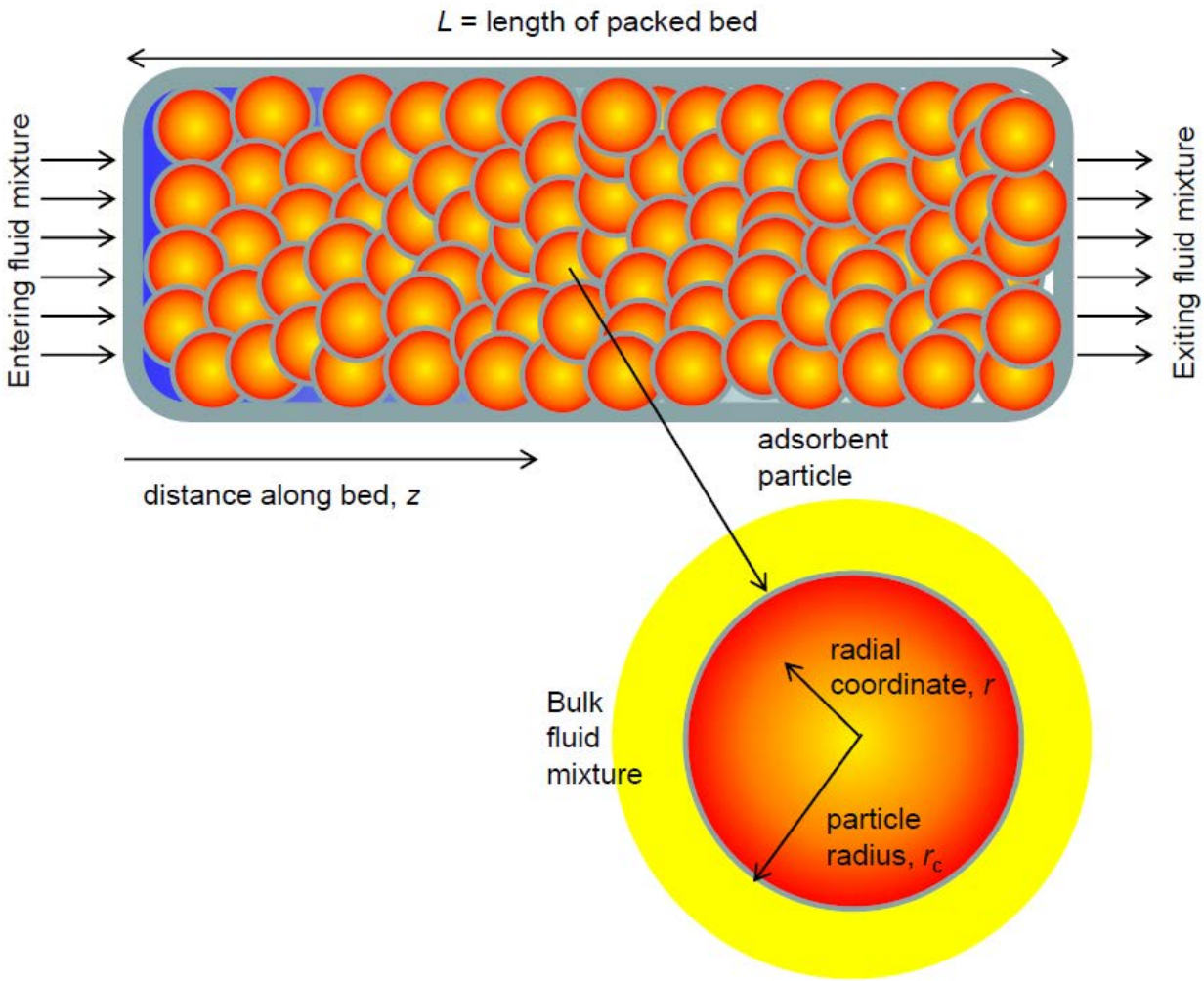

Figure S8. Schematic of fixed bed adsorber filled with adsorbent particles of radius r_c.

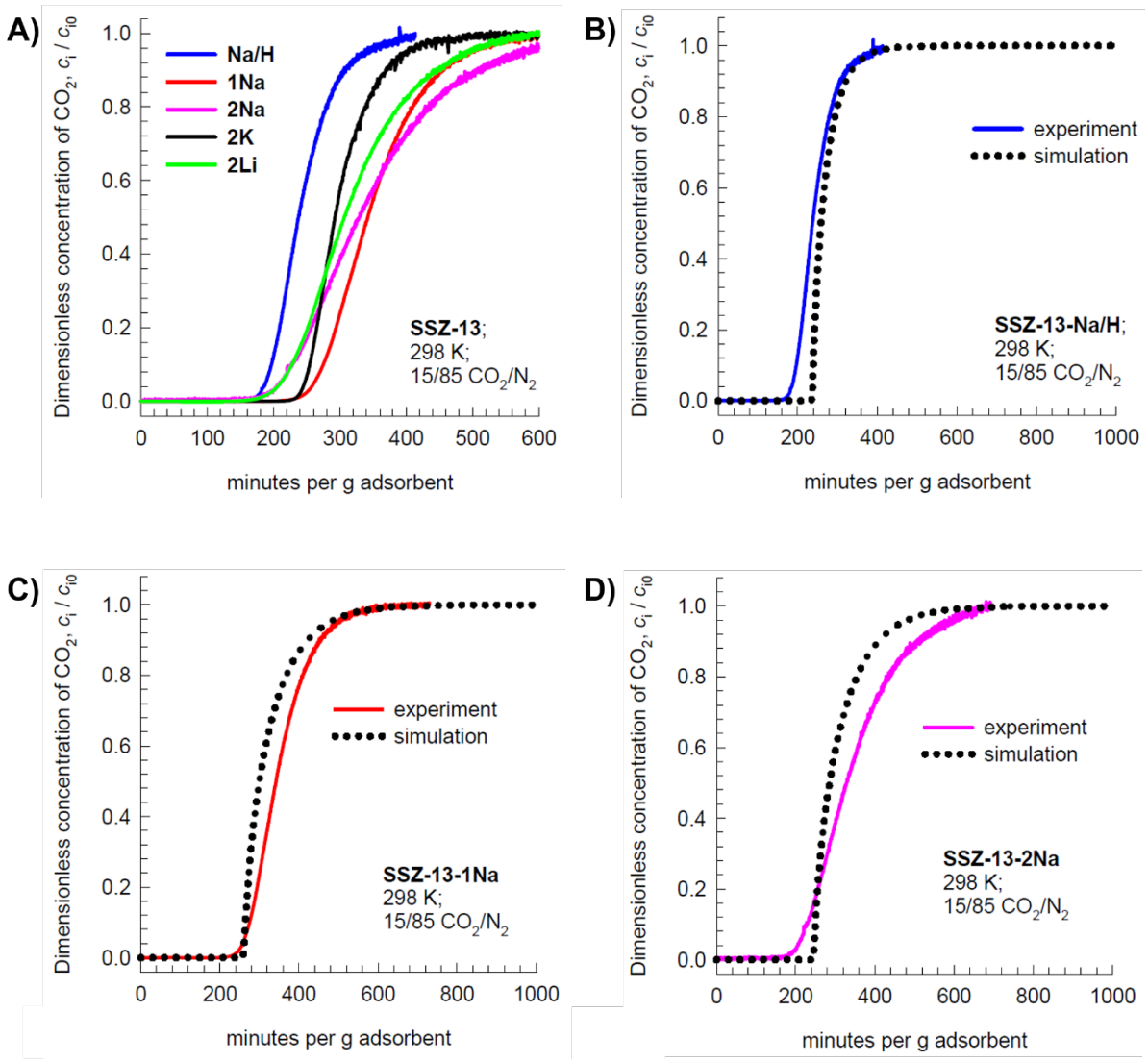
A)
Dimensionless concentration of CO2, ci / ci0
1.0
0.8
0.6
0.4
0.2
0.0
0
100
200
300
400
500
600
minutes per g adsorbent
Na/H
1Na
2Na
2K
2Li
SSZ-13;
298 K;
15/85 CO2/N2
B)
Dimensionless concentration of CO2, ci / ci0
1.0
0.8
0.6
0.4
0.2
0.0
0
200
400
600
800
1000
minutes per g adsorbent
experiment
simulation
SSZ-13-Na/H;
298 K;
15/85 CO2/N2
C)
Dimensionless concentration of CO2, ci / ci0
1.0
0.8
0.6
0.4
0.2
0.0
0
200
400
600
800
1000
minutes per g adsorbent
experiment
simulation
SSZ-13-1Na
298 K;
15/85 CO2/N2
D)
Dimensionless concentration of CO2, ci / ci0
1.0
0.8
0.6
0.4
0.2
0.0
0
200
400
600
800
1000
minutes per g adsorbent
experiment
simulation
SSZ-13-2Na
298 K;
15/85 CO2/N2

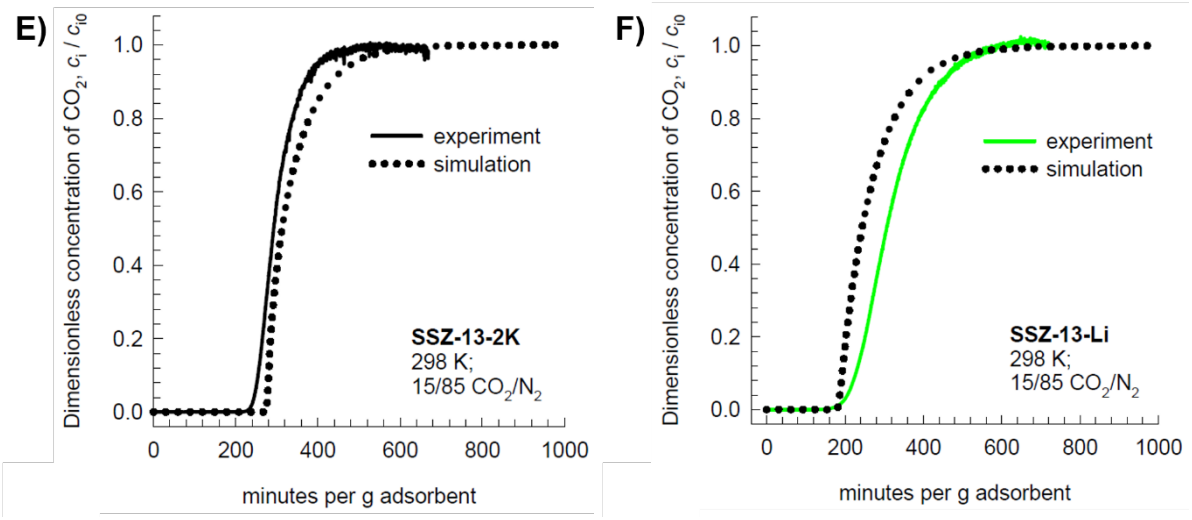

Figure S9. (a) Experimental data on breakthroughs for 15/85 CO_2/N_2 mixtures at 298 K, and 100 kPa showing the dimensionless concentrations of CO_2 at the outlet for Na/H, 1Na, 2Na, 2K, and 2Li adsorbents. (b, c, d, e, f) Comparison of experimental data on breakthroughs for (b) Na/H, (c) 1Na, (d) 2Na, (e) 2K, and (f) 2Li adsorbents with transient breakthrough simulations taking $\frac{Đ_{CO2}}{r_c^2} = 2\times10^{-4}$ s^{-1}, and $\frac{Đ_{N2}}{r_c^2} = 2\times10^{-3}$ s^{-1}.

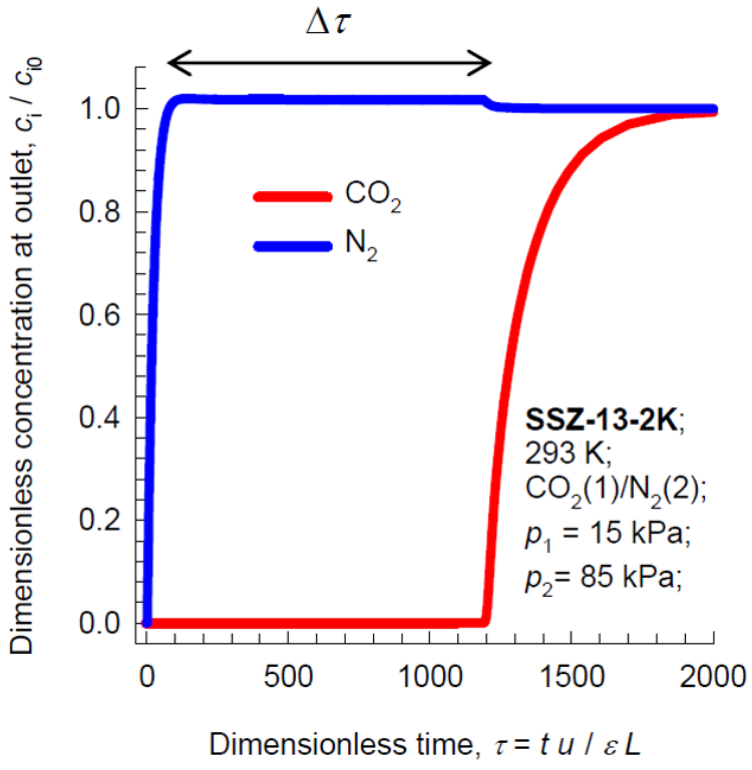
Δτ
Dimensionless concentration at outlet, c_i / c_{i0}
1.0
0.8
0.6
0.4
0.2
0.0
CO2
N2
SSZ-13-2K;
293 K;
CO2(1)/N2(2);
p1 = 15 kPa;
p2= 85 kPa;
0
500
1000
1500
2000
Dimensionless time, τ = t u / ε L

Figure S10. Transient breakthrough simulations for 15/85 CO_2/N_2 mixtures at 298 K, and 100 kPa in a fixed bed packed with 2K-SSZ-13.

References

(1) Prodinger, S.; Derewinski, M. A.; Wang, Y.; Washton, N. M.; Walter, E. D.; Szanyi, J.; Gao, F.; Wang, Y.; Peden, C. H. F., Sub-micron Cu/SSZ-13: Synthesis and application as selective catalytic reduction (SCR) catalysts. Applied Catalysis B: Environmental 2017, 201, 461-469.

(2) Smith, L. J.; Eckert, H.; Cheetham, A. K. Potassium cation effects on site preferences in the mixed cation zeolite Li, Na-chabazite. Chem. Mater. 2001, 13 (2), 385−391.

(3) Prodinger, S.; Vemuri, R. S.; Varga, T.; McGrail, B. P.; Motkuri, R. K.; Derewinski, M. A., Impact of chabazite SSZ-13 textural properties and chemical composition on CO_2 adsorption applications. New J. Chem. 2016, 40 (5), 4375-4385.

(4) Gao, F.; Wang, Y.; Kollár, M.; Washton, N. M.; Szanyi, J.; Peden, C. H. F., A comparative kinetics study between Cu/SSZ-13 and Fe/SSZ-13 SCR catalysts. *Catal. Today* **2015,** *258, Part 2*, 347-358.

(5) Rouquerol, J.; Llewellyn, P.; Rouquerol, F., Is the bet equation applicable to microporous adsorbents? Stud. Surf. Sci. Catal. 2007, 160, 49-56.

(6) Myers, A. L.; Prausnitz, J. M. Thermodynamics of Mixed Gas Adsorption. A.I.Ch.E.J. 1965, 11, 121-130.

(7) Krishna, R. Screening Metal-Organic Frameworks for Mixture Separations in Fixed-Bed Adsorbers using a Combined Selectivity/Capacity Metric. RSC Adv. 2017, 7, 35724-35737.

(8) Krishna, R. The Maxwell-Stefan Description of Mixture Diffusion in Nanoporous Crystalline Materials. Microporous Mesoporous Mater. 2014, 185, 30-50.

(9) Krishna, R. Methodologies for Evaluation of Metal-Organic Frameworks in Separation Applications. RSC Adv. 2015, 5, 52269-52295.

(10) Krishna, R.; Baur, R. Modelling Issues in Zeolite Based Separation Processes. Sep. Purif. Technol. 2003, 33, 213-254.

(11) Krishna, R.; Long, J. R. Screening metal-organic frameworks by analysis of transient breakthrough of gas mixtures in a fixed bed adsorber. J. Phys. Chem. C 2011, 115, 12941-12950.

(12) Pham, T. D.; Liu, Q.; Lobo, R. F., Carbon Dioxide and Nitrogen Adsorption on Cation-Exchanged SSZ-13 Zeolites. Langmuir 2013, 29 (2), 832-839.

(13) Belmabkhout, Y.; Pirngruber, G.; Jolimaitre, E.; Methivier, A. A complete experimental approach for synthesis gas separation studies using static gravimetric and column breakthrough experiments. Adsorption 2007, 13, 341-349.

(14) Cavenati, S.; Grande, C. A.; Rodrigues, A. E. Adsorption Equilibrium of Methane, Carbon Dioxide, and Nitrogen on Zeolite 13X at High Pressures. J. Chem. Eng. Data 2004, 49, 1095-1101.